Reflectance Measurements for Black Absorbers Made of Vertically Aligned Carbon Nanotubes

X. J. Wang, O. S. Adewuyi, L. P. Wang, B. A. Cola, and Z. M. Zhang*
George W. Woodruff School of Mechanical Engineering
Georgia Institute of Technology
Atlanta, GA 30332, USA

ABSTRACT

Black coatings have important applications in space-borne infrared systems, absolute radiometers, and radiometric temperature measurements. Recently, researchers have demonstrated close-to-unity absorptance, with diffuse reflection, by using vertically aligned carbon nanotube (VACNT) arrays. The present study deals with the optical properties of highly absorbing VACNT arrays, with surface features from diffuse to specular. Three CNT arrays were fabricated using a thermal chemical vapor deposition (CVD) technique with different growth conditions to produce highly aligned multi-walled CNT arrays. The bidirectional reflectance distribution functions (BRDFs) were measured with a laser scatterometer at a wavelength of 635 nm. Sharp specular peaks can be seen from the BRDF plots for the relatively smooth sample; while for the relatively diffuse samples, the specular peaks are significantly lower. The directional-hemispherical reflectance (DHR) at wavelengths from 400 to 1000 nm was measured with an integrating sphere and a monochromator. Based on Kirchhoff's law, the absorptance was obtained from the DHR to be between 99.5% and 99.9% for all samples in the measured spectral region.

Keywords: Black Absorber, BRDF, Carbon Nanotubes, Reflectance

1. INTRODUCTION

Black materials with low reflectivity have numerous applications; for instance, high-efficiency absorbers or emitters for energy conversion, radiometers and bolometers for space-borne infrared systems, calibration standards and backing materials for radiation measurements, and light trappers in optical systems.[1-5] Extremely high absorption has been achieved with vertically aligned carbon nanotubes (VACNTs), due to their intrinsic material properties as well as the sparse tube-to-tube spacing.[6-10] Geohegan et al.[11] performed *in situ* laser measurements of VACNTs, and observed a reduction of specular reflectance as time evolves due to absorption and scattering. Yang et al.[6] reported an extremely dark, Lambertian-like material made by a low-density CNT array. Wang et al.[7] studied the radiative properties of CNT arrays fabricated using both the tip-growth and base-growth mechanisms. Most of the CNT arrays involved in pertinent studies are diffuse reflectors, presumably due to surface roughness and inhomogenuity in the arrays. While materials with diffuse surfaces may have omnidirectional reflection/absorption, materials with specular surfaces are also desirable for certain applications, such as baffles designed for specular vane surfaces and blackbody cavities.[1,12] Although some conventional black paints or appliqués exhibit specular reflection,[1,5] highly absorbing CNT arrays with specular reflection have not been reported.

The present paper reports an experimental investigation of VACNTs of high absorptance in the visible and infrared and with various surface features from nearly specular to highly diffuse. The bidirectional reflectance distribution functions (BRDFs) of the CNT samples fabricated using thermal chemical vapor deposition (CVD) were measured using a laser scatterometer. The directional-hemispherical reflectance (DHR) in the spectral range from 400 to 1000 nm was obtained using an integrating sphere. The sample fabrication, characterization, optical instrumentation, and measurement results are discussed in subsequent sections, followed by a summary.

* Corresponding author: zhuomin.zhang@me.gatech.edu.

2. SAMPLE FABRICATION AND CHARACTERIZATION

Three vertically aligned multi-walled CNT samples were synthesized on 100-mm-diameter Si wafers by thermal CVD using an Axitron Black Magic system. Metal stacks of 30-nm Ti, 10-nm Al, and 3-nm Fe were deposited on the Si wafers to form a trilayer catalyst for CNT growth.[13] The process gases were C_2H_2 and H_2 mixed at the flow rates of 100 and 160 standard cubic centimeters per minute (sccm) for Samples 1 and 3. While for Sample 2, the flow rates for C_2H_2 and H_2 gases were 100 and 700 sccm, respectively. N_2 was used as a carrier gas with variable flow rates. The growth pressure measured before the gas exit into the vacuum pump was 70 kPa for Samples 1 and 3, and 0.13 kPa for Sample 2. The growth time was 10 min for Samples 1 and 2, and 2 min for Sample 3. The substrate temperature was maintained at 750°C during the CNT growth for all three samples. The samples were diced into smaller pieces before the scanning electron microscopy (SEM) imaging and integrating sphere measurements. For BRDF measurements, most samples were measured both before dicing and after dicing at similar locations on the sample. Based on the SEM images, the average thicknesses of Samples 1 to 3 statistically estimated from random locations (around 40 locations for each sample) were approximately as 166 μm, 48 μm, and 34 μm, respectively. The density was obtained by weighing the mass of the CNTs using an analytic balance and measuring the covering areas of the substrates. The volume fraction, defined as the ratio of the volume occupied by CNTs to the total volume of the array, can be calculated by comparing the CNT array density to the graphite density which is taken as 2.2 g/cm^3. Table 1 lists the fabrication conditions as well as the parameters of each sample. From Table 1, the sample thickness is larger with a longer growth time but the relationship between thickness and growth time is not linear. In addition, when the growth time stays the same, pressure and gas flow rate of H_2 seem to affect the mass of deposited CNTs. The uncertainties of density and volume fraction are estimated based on a 10% thickness uncertainty and 10% area uncertainty due to the somewhat irregular shape and the substrate is not fully covered with CNTs. The mass uncertainty is estimated less than 7% based on the instrument resolution. The relative uncertainty of density is around 15% mainly due to the uncertainties in thickness and area.

Table 1. Growth conditions and measured parameters for the samples.

Sample Number	**Pressure (kPa)**	**Process Gas Flow Rate, C_2H_4 : H_2 (sccm)**	**Growth Time (min)**	**Thickness (μm)**	**Density (g/cm^3)**	**Volume Fraction (%)**
1	70	100 : 160	10	166 ± 16	0.067 ± 0.010	3.0 ± 0.5
2	0.13	100 : 700	10	48 ± 5	0.129 ± 0.019	5.9 ± 0.9
3	70	100 : 160	2	34 ± 3	0.190 ± 0.028	8.6 ± 1.3

Figure 1 displays three representative SEM images of the fabricated CNT samples. Figure 1(a) shows the side view of Sample 1. Although some CNTs near the edge are curved and twisted due to wafer dicing, the CNTs with a thickness of around 160 μm are shown to be well aligned and very uniform. Due to the resolution limit of the SEM imaging, it is hard to distinguish differences between individual samples based on the side view of the entire arrays; hence, only Sample 1 is selected as the representative. Figures 1(b) and 1(c) are inclined views near the top of Samples 1 and 2, respectively, with nearly the same magnification as indicated by the scale bars. Sample 1 has a fairly flat surface formed by the tube tips and the array is pretty uniform as shown by the edge. When Sample 2 is viewed from the side along the edge, the array uniformity is comparable with that of Sample 1. However, its surface appears cloudy and wavy over a large area, suggesting the surface of Sample 2 is relatively rough. Since the top view of Sample 3 with the same magnification has similar features as that of Sample 2, its images are not presented here. In addition, when these samples are examined by naked eyes, the surface of Sample 1 is shinny and displays different colors when the angle of observation is varied; the surface of Sample 2 is dark color and not as smooth; the surface of Sample 3 is purely dark, diffuse, and nearly isotropic when tilted. The trend in appearance suggests that Sample 1 is more specular, presumably due to the better uniformity, smoothness, and alignment.

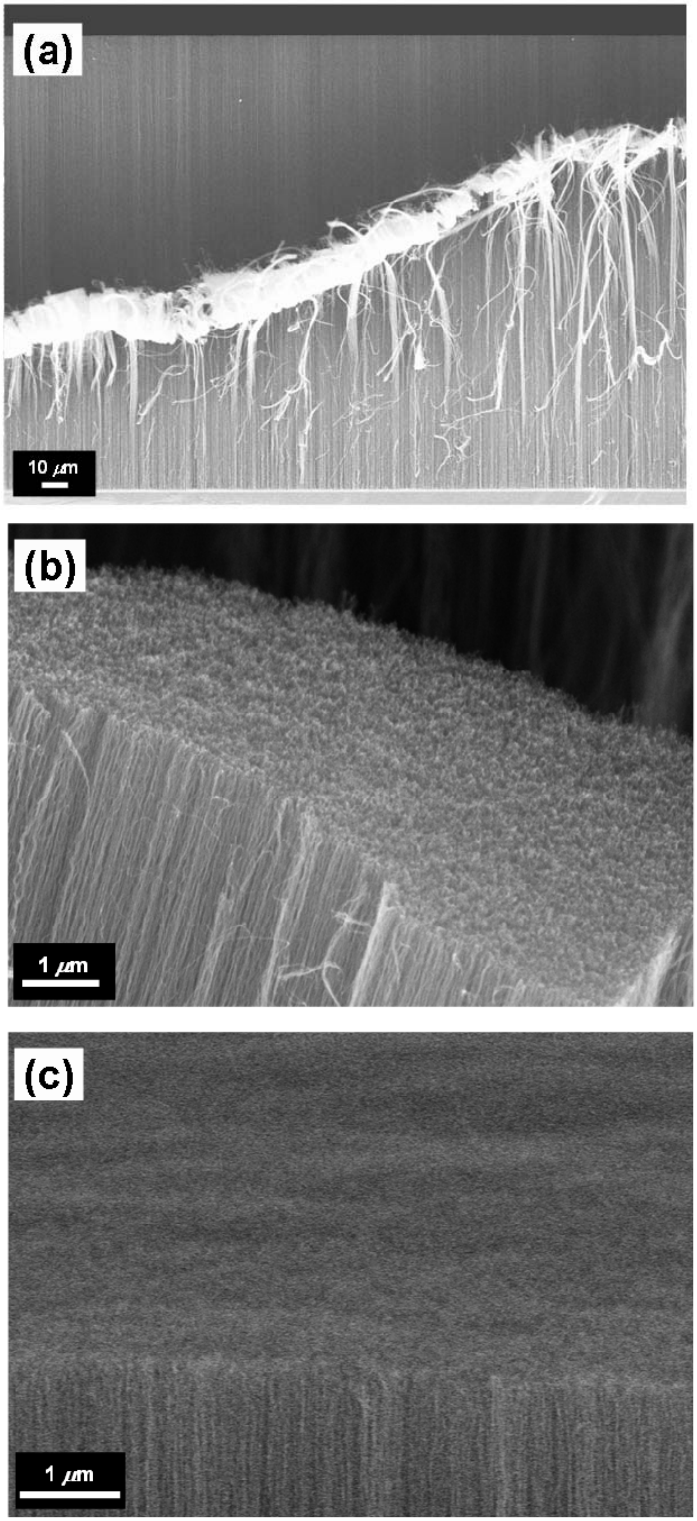

Figure 1. Representative SEM images: (a) Side view of Sample 1, (b) Inclined view of Sample 1 whose side is well aligned and top is relatively smooth, (c) Inclined view of Sample 2 whose surface is less smooth. The scale bars correspond to different magnifications.

3. MEASUREMENT INSTRUMENTATION

A three-axis automated scatterometer (TAAS) was used to measure the BRDF of the CNT arrays, which is defined as the ratio of the reflected radiance to the incident irradiance,[14]

$$f_{\mathrm{r}}(\lambda,\theta_{\mathrm{i}},\phi_{\mathrm{i}},\theta_{\mathrm{r}},\phi_{\mathrm{r}}) = \frac{dI_{\mathrm{r}}}{I_{\mathrm{i}}\cos\theta_{\mathrm{i}}\delta\Omega_{\mathrm{i}}} \quad [\mathrm{sr}^{-1}] \tag{1}$$

where θ and ϕ specify the beam direction, with the subscripts "i" and "r" denoting the incident and reflected beams, respectively, $\delta\Omega_{\mathrm{i}}$ is the solid angle of the incident beam, I_{i} is the incident radiance and dI_{r} is the reflected radiance. Considering that the detector signal is proportional to the radiant power collected by the detector, BRDF can be related to the measured quantities using the following measurement equation,[15,16]

$$f_{\mathrm{r}} = C\frac{P_{\mathrm{sig}}}{P_{\mathrm{ref}}\cos\theta_{\mathrm{r}}\delta\Omega_{\mathrm{r}}} \tag{2}$$

where P_{sig} and P_{ref} are the powers received by the signal detector and the reference detector, respectively, $\delta\Omega_{\mathrm{r}}$ is the solid angle of the signal detector viewed from the sample, and C is a constant to compensate for the beamsplitter ratio and the different detector responsivities. It should be noted that the detector solid angle in TAAS is 0.000184 sr, which corresponds to a half cone angle of 0.45°.

Figure 2(a) shows a schematic of the TAAS setup as viewed from the top of the optical table. A 635-nm diode laser provides highly collimated incident beam. The beam can be polarized as either TE (*s* polarization) or TM (*p* polarization) waves by a linear polarizer, and is then divided into two portions by a beamsplitter. The transmitted portion with a higher power reaches the sample and the reflected portion with a lower power reaches the reference detector. The sample is attached to one movable stage of TAAS located on a goniometric table, which allows the sample and the signal detector to be rotated using two step motors. Another step motor is available to rotate the detector out of the incidence plane, but is not used in the present study. The goniometric table and the laser system are mounted on an optical table. The signals collected by both detectors are magnified by two trans-impedance preamplifiers with large dynamic ranges for low-level power measurements. A lock-in amplifier is used to pick up the signal after each preamplifier at 400 Hz, which is synchronized with the modulation frequency of the laser driver. A black screen with an opening is used to separate the optical source and the goniometric table, as shown in Fig. 2(a). Additional screens and light trappers are used to prevent stray light from reaching the sample or the signal detector.

Figures 2(b) and 2(c) describe the setup of the DHR measurements using the center-mount and back-mount configurations, respectively. The inner wall of the integrating sphere is coated with a diffuse white reflector, polytetrafluoroethylene (PTFE). The light source is a grating monochrometer with a tungsten halogen lamp. It can provide narrow band (with 10 nm resolution) radiation from ultraviolet to near infrared using two gratings and a set of filters. In the center-mount configuration, the incident beam can be focused on to the sample suspended in the sphere's center through a rotatable sample holder.[17] A reference made of the same material as the sphere wall is located at the back port of the sphere. For the background signal measurement, the sample is rotated by 90° so that the beam bypasses the sample and strikes the reference (located on the back port of the integrating sphere). For the sample reflection signal measurement, the sample is tilted by about 7° so that the light that is specularly reflected by the sample surface will not escape the sphere through the entrance port. The ratio of sample signal and background signal gives the reflectance of the sample. A Si detector mounted at the bottom of the sphere below a baffle is used along with a preamplifier, a lock-in amplifier, and a chopper.

For back-mount configuration, the illumination source is a 635-nm diode laser as used for measuring the BRDFs. The CNT sample is mounted on the back port in a way that both the sample and the reference cover half of the back port, as shown in Fig. 2(c).[18] The sample or background signal is collected by directing the laser beam to either the sample or the reference separately. No chopper is needed with the laser since the output power is modulated by the driver current. Due to the length of the optical path, it is difficult to focus the light out from the monochromater to the back port.

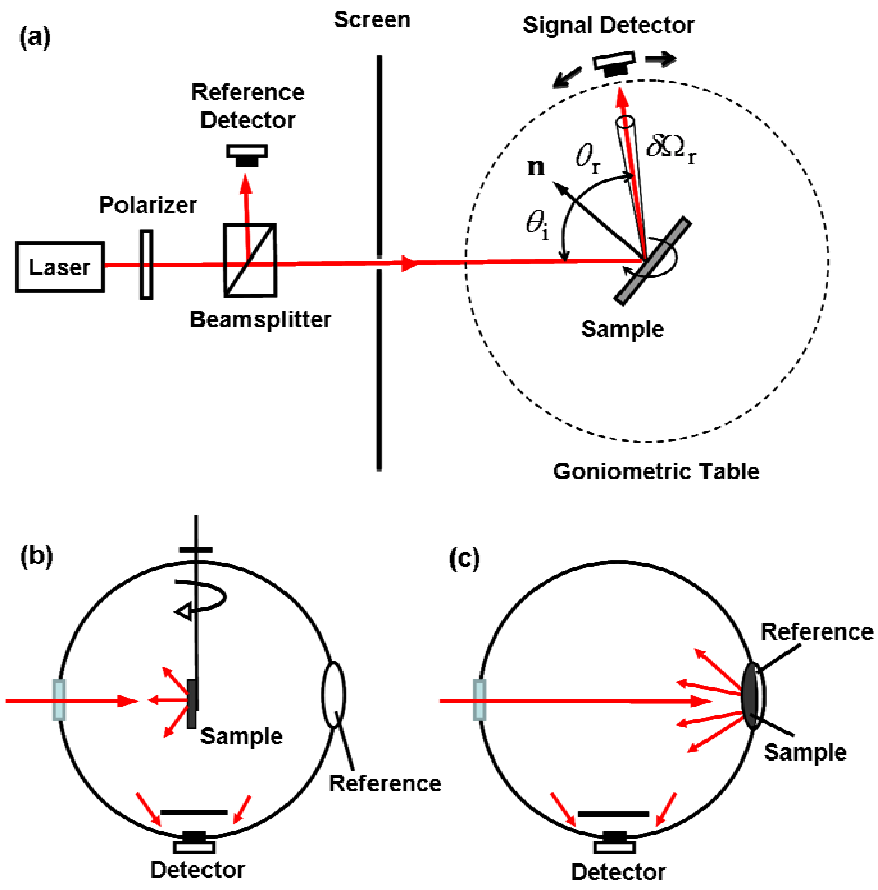

Figure 2. Schematics of the measurement setups: (a) TAAS for in-plane BRDF measurements; (b) Integrating sphere with tungsten halogen lamp as the light source using center-mount configuration for spectral DHR measurements; (c) Integrating sphere with a diode laser as the light source using back-mount configuration for measuring DHR at 635 nm.

4. RESULTS AND DISCUSSION

The incidence angles for BRDF measurements were set to be 0°, 30°, and 60°. The measured BRDFs of all three samples for both polarizations are plotted in Fig. 3. For easier comparison, the cosine corrected BRDFs, f_r*cos(θ_r), for all three samples are plotted on the *y*-axis with the same scale. Since the interest of this study is to investigate the BRDF of the VACNT arrays near the specular peaks, only the forward reflectance were considered within a certain range of θ_r around the direction of specular reflection. The interval of the reflection angles was taken as 0.2° near the specular reflection angle and 5° for off-specular measurements. At normal incidence, the BRDFs within ±3° of the specular direction could not be measured due to the blockage of the incident beam by the signal detector. Therefore, the BRDFs within ± 3° around the normal direction were obtained by shifting the specular peak at θ_i = 4° by the peak reflection angle of 4°. One the other hand, the average values of BRDFs measured within two ranges of θ_r from –80° to –3° and from 3° to 80° were taken as the BRDFs corresponding to θ_r from 3° to 80° at normal incidence. In order to reduce the random error, P_{sig} and P_{ref} were averaged over 30 measurements for each position. For the specular peaks in Sample 1, the standard deviation is within 5%, but for very small BRDF values, the standard deviation of the 30 measurements can be as large as 30% due to the low signal-to-noise ratio. Additional uncertainty sources could arise from misalignment, stray light, and variation at different locations on the same sample. Hence, the expanded uncertainty is estimated to be about 10% when f_r*cos(θ_r) is greater than 10 sr^{-1} and increases to about 40% when f_r*cos(θ_r) is below 0.001 sr^{-1}.

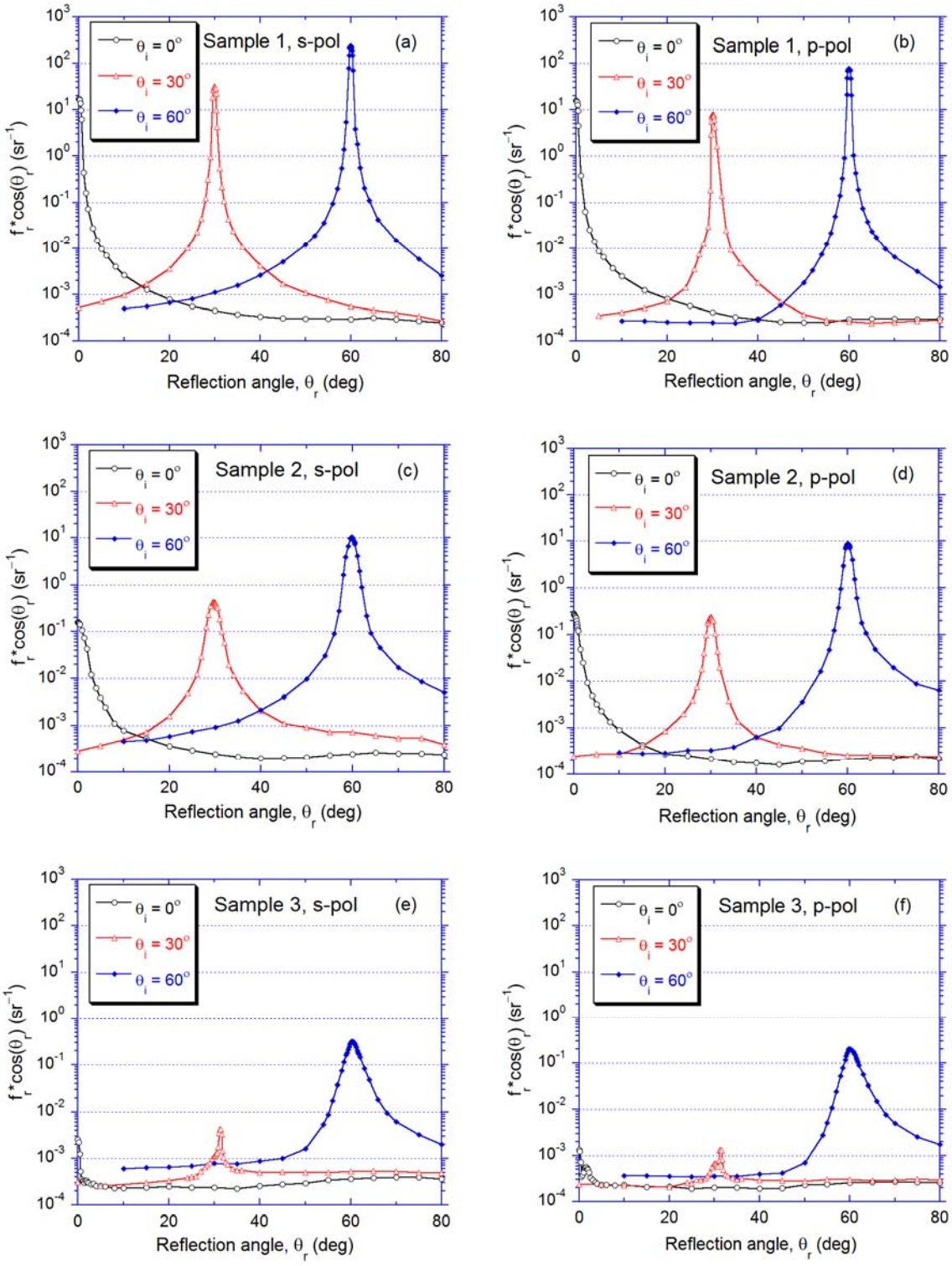

Figure 3. BRDFs measured at 635 nm wavelength for all three samples at incidence angles of 0^o, 30^o, and 60^o. In the figures, s-pol and p-pol represent, respectively, *s* polarization and *p* polarization. The specular peaks at normal incidence are obtained by shifting the measured BRDF at 4^o incidence angle.

Specular peaks at $\theta_r = \theta_i$ can be seen from Fig. 3, with different magnitudes and sharpness for individual samples. For Sample 1, the corrected BRDF drops more than 5 orders of magnitude from the peak to the smallest values; while for Sample 2, the peaks are about one order of magnitude lower than those of Sample 1. As for Sample 3, the peaks at near normal incidence are obscure and these at oblique incidence are much lower and broader that those for Sample 2. The sharpness of specular peaks in BRDF for different samples is consistent with their appearance and SEM images. At (near) normal incidence, the full width at half maximum of the specular peak for Sample 1 is less than 1^o. In addition, within $\pm 2^o$, the BRDF of Sample 1 is reduced by 2 orders of magnitude from the peak value. The width and sharpness of BRDF for Sample 1 are comparable with those of Chemglaze Z302 (also known as Aeroglaze Z302), a typical specular black paint used in high-accuracy radiometers,[19] as measured by Snail et al..[5] However, the BRDF for Sample 1 at large reflection angles is about a factor of 2 to 4 lower than that for Chemglaze Z302, suggesting that Sample 1 has an even lower reflectance or higher absorptance. Also, the peak magnitudes are higher for *s* polarization than for *p* polarization for all samples; this is consistent with the Fresnel reflection at a smooth interface. For Sample 3, the magnitudes of specular peak at $\theta_i = 0^o$ and 30^o are on the order of 10^{-3}, but suddenly increases by 2 orders of magnitude at $\theta_i = 60^o$, indicating the diffuse sample tends to be more specular at large incidence. This suggests that light scattering from these CNT samples is dominated by surface roughness and at larger incidence angles, the surface appears less rough.

For the DHR measurements using the integrating sphere, calibration and measurement uncertainties are important. The theories and correction methods for the integrating sphere have been extensively discussed by Hanssen.[18,20] In an earlier study,[17] calibration of the center-mount configuration was done with a silicon wafer, whose reflectance is greater than 50%. For highly absorbing samples, however, a large portion of the optical energy that is multiply reflected by the sphere wall may be absorbed by the sample itself. The fraction that is absorbed may not be fully compensated between the background measurement and the sample measurement, since the sample orientation is different and the sample is neither ideally specular nor perfectly diffuse. It is found that a large sample (about 25×25 mm^2) would give a much lower reflectance. By reducing the sample size to approximately 18×18 mm^2, the measured reflectance was increased by 30% to 50%. The DHR measured with center-mount configuration using the diode laser is very close to that obtained using the monochromator at 635 nm wavelength. On the other hand, when the measurement is compared to that obtained with back-mount configuration using the diode laser, the measured reflectance is increased by 25% to 35%, which is closer to the DHR calculated by integrating the BRDF at normal incidence, under the assumption that the CNT samples are optically symmetric with respect to the azimuthal angle. However, it is difficult to focus the monochromator light to the sample in the back-mount configuration due to the limit of beam size in the current setup. In addition, the back-mount configuration is subject to its own uncertainties; therefore, from the laser measurement and the standard deviations, it is estimated that the spectral DHR measurements have a relative uncertainty of 30%, which results in only 0.1% to 0.2% relative uncertainties in the absorptance ($\alpha = 1 - R$) using Kirchhoff's law. The DHR and absorptance at 635 nm wavelength obtained from different methods are summarized in Table 2.

Figure 4 shows the spectral DHR measurements from 400 to 1000 nm for samples with reduced sizes using the center-mount configuration. The laser measurement results using back-mount configuration are shown as marks in Fig. 4. The error bars for 30% relative uncertainty are labeled at three wavelengths of 500, 700, and 900 nm for different samples. Since the spectral resolution is very high (10 nm interval in wavelength), the DHR spectral measured with the monochromator are shown as continues curves. Within the measured spectral region, Sample 3 has the lowest reflectance ranging from 0.0007 to 0.002, followed by Sample 2 whose DHR ranges from 0.001 to 0.002. On the other hand, Sample 1 has the highest DHR, ranging from 0.003 to 0.005. The DHR for Sample 1 exhibits some interference fringes, which are attributed to the density variation near the tip of the CNTs, within 1-2 μm thickness near the surface of the CNT array. However, similar phenomenon is not observed for Samples 2 and 3 due to the reduction of coherence when light gets reflected by rougher surfaces.[14] The interference effect explains the glossy and colorful appearance of the surface of Sample 1 as seen by eyes. It is worth noting that the DHR for Sample 3 tends to decrease as wavelength gets longer; this may be due to the fact that scattering by roughness becomes weaker at longer wavelength.[7,21] Other effects such as the change of the effective refractive index and the effective surface roughness may also play a role. The trend for Sample 2 is not as distinguishable, but the DHR slightly increase with wavelength as opposite to that for Sample 3.

Table 2. DHR (R) and absorptance of the samples obtained using different methods at 635 nm wavelength.

Sample Number	Center Mounting		Back Mounting		BRDF Integration	
	R (%)	α (%)	R (%)	α (%)	R (%)	α (%)
1	0.42	99.58	0.58	99.43	0.64	99.36
2	0.16	99.84	0.20	99.80	0.21	99.79
3	0.10	99.90	0.13	99.87	0.18	99.82

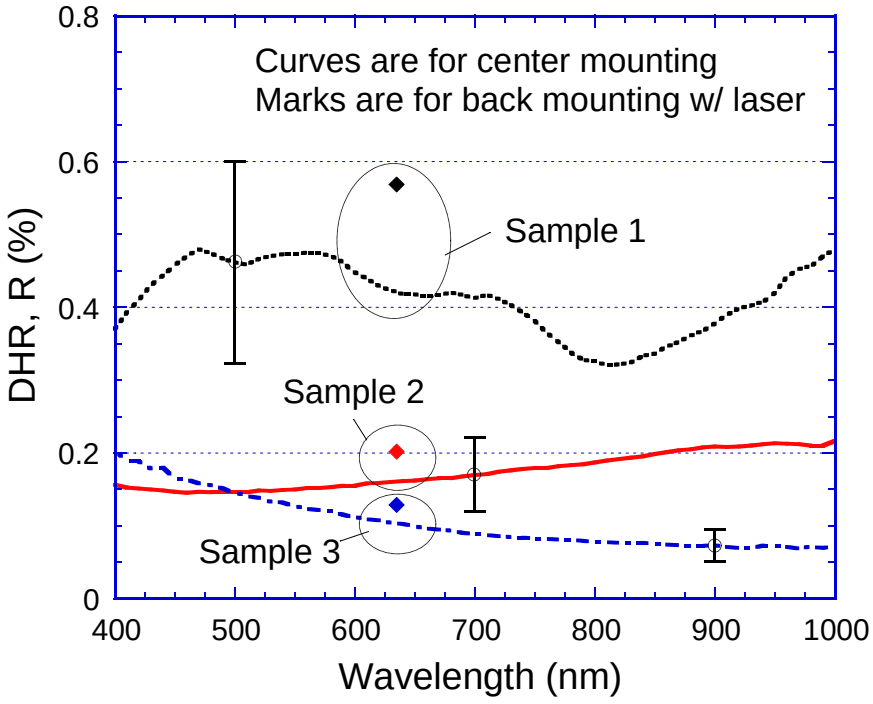

Figure 4. Spectral DHR measured using integrating sphere with center-mount configuration (curves) and back-mount configuration (marks). The sample was cut to about 18 × 18 mm^2 in size to compensate the difference in the sample signal and background signal. The error bars represent an expended uncertainty of 30%.

5. CONCLUSIONS AND FUTURE WORK

In summary, three vertically aligned multi-walled CNT arrays with different surface roughnesses are fabricated by varying the growth conditions. The optical properties of the CNT samples are examined by measuring the BRDFs at the wavelength of 635 nm and the DHR within the wavelength region from 400 to 1000 nm. Specular peaks with different magnitudes and widths are observed from the measured BRDFs. The sharpness of the peak around the specular direction indicates the surface roughness variation of the CNT samples from nearly specular to highly diffuse. The high absorption of the CNT samples is demonstrated by the near unity (0.995-0.999) absorptance obtained from the DHR measurements. The specular surface of CNT samples is attributed to the excellent alignment and sample uniformity. Future works are needed to correlate growth parameters during CNT fabrication and resulting CNT array morphology (e.g., density, alignment, and surface roughness) with the optical properties of CNT arrays.

ACKNOWLEDGMENTS

XJW, LPW, and ZMZ acknowledge the support from the National Science Foundation (CBET-0828701). OSA and BAC acknowledge support from the Defense Advanced Research Projects Agency NTI program, Georgia Tech's Woodruff School of Mechanical Engineering and Nanotechnology Research Center. Mr. Sheng Xu of Georgia Tech's School of Materials Science and Engineering is appreciated for help taking the SEM images.

REFERENCES

[1] Persky, M. J., "Review of black surfaces for space-borne infrared systems," Rev. Sci. Instrum. 70, 2193-2216 (1999).

[2] Betts, D. B., Clarke, F. J. J., Cox, L. J., and Larkin, J. A., "Infrared reflection properties of five types of black coating for radiometric detectors," J. Phys. E 18, 689-696 (1985).

[3] Zhang, Z. M., Tsai, B. K., and Machin, G., *Radiometric Temperature Measurements: I & II*, Academic Press, Amsterdam (2010).

[4] Wightman, T. E., and Grum, F., "Low-reflectance backing materials for use in optical radiation measurements," Color Res. Appl. 6, 139-142 (1981).

[5] Snail, K. A., Brown, D. P., Costantino, J., Shemano, W. C., Schmidt, C. W., Lynn, W. F., Seaman, C. L., and Knowles, T. R., "Optical characterization of black appliques," Proc. SPIE 2864, 465-474 (1996).

[6] Yang, Z.-P., Ci, L., Bur, J. A., Lin, S.-Y., and Ajayan, P. M., "Experimental observation of an extremely dark material made by a low-density nanotube array," Nano Lett. 8, 446-451 (2008).

[7] Wang, X. J., Flicker, J. D., Lee, B. J., Ready, W. J., and Zhang, Z. M., "Visible and near-infrared radiative properties of vertically aligned multi-walled carbon nanotubes," Nanotechnology 20, 215704 (2009).

[8] Mizuno, K., Ishii, J., Kishida, H., Hayamizu, Y., Yasuda, S., Futaba, D. N., Yumura, M., and Hata, K., "A black body absorber from vertically aligned single-walled carbon nanotubes," PNAS 106, 6044 - 6047 (2009).

[9] Camacho, R. E., Morgan, A. R., Flores, M. C., McLeod, T. A., Kumsomboone, V. S., Mordecai, B. J., Bhattacharjea, R., Tong, W., Wagner, B. K., Flicker, J. D., Turano, S. P., and Ready, W. J., "Carbon nanotube arrays for photovoltaic applications," JOM 59, 39-42 (2007).

[10] Lehman, J. H., Deshpande, R., Rice, P., To, B., and Dillon, A. C., "Carbon multi-walled nanotubes grown by HWCVD on a pyroelectric detector," Infrared Phys. Technol. 47, 246-250 (2006).

[11] Geohegan, D. B., Puretzky, A. A., Ivanov, I. N., Jesse, S., Eres, G., and Howe, J. Y., "In situ growth rate measurements and length control during chemical vapor deposition of vertically aligned multiwall carbon nanotubes," Appl. Phys. Lett. 83, 1851 (2003).

[12] Peterson, G. L., Johnston, S. C., and Thomas, J., "Specular baffles," Proc. SPIE 1753, 65-76 (1992).

[13] Xu, J., and Fisher, T. S., "Enhancement of thermal interface materials with carbon nanotube arrays," Int. J. Heat Mass Transfer 49, 1658-1666 (2006).

[14] Zhang, Z. M., *Nano/Microscale Heat Transfer*, McGraw-Hill, New York (2007).

[15] Shen, Y. J., Zhu, Q. Z., and Zhang, Z. M., "A scatterometer for measuring the bidirectional reflectance and transmittance of semiconductor wafers with rough surfaces," Rev. Sci. Instrum. 74, 4883-4892 (2003).

[16] Lee, H. J., and Zhang, Z. M., "Measurement and modeling of the bidirectional reflectance of SiO_2 coated Si surfaces," Int. J. Thermophys. 27, 820-839 (2006).

[17] Lee, H. J., Bryson, A. C., and Zhang, Z. M., "Measurement and modeling of the emittance of silicon wafers with anisotropic roughness," Int. J. Thermophys. 28, 918-933 (2007).

[18] Hanssen, L. M., and Snail, K. A., "Integrating spheres for mid-and near-infrared reflection spectroscopy," in *Handbook of Vibrational Spectroscopy*, Vol. 2, pp. 1175-1192, J. M. Chalmers and P. R. Griffiths (eds.), Wiley, New York (2002).

[19] Zhang, Z. M., Datla, R. U., Lorentz, S. R., and Tang, H. C., "Thermal modeling of absolute cryogenic radiometers," J. Heat Transfer 116, 993-998 (1994).

[20] Hanssen, L., "Integrating-sphere system and method for absolute measurement of transmittance, reflectance, and absorptance of specular samples," Appl. Opt. 40, 3196-3204 (2001).

[21] Bohren, C. F., and Huffman, D. R., *Absorption and Scattering of Light by Small Particles*, Wiley, New York (1983).